In-Orbit Two-Dimensional Feed-Array Pattern Measurement for Digital Beamforming SAR Using a Double-Cross-Helix Formation

Josef Mittermayer[a], Gerhard Krieger[a], Michelangelo Villano[a]
[a] German Aerospace Center (DLR), Oberpfaffenhofen, 82234 Wessling, Germany

Abstract

The paper introduces the in-orbit antenna pattern measurement by a dedicated small measurement satellite flying in Double-Cross-Helix formation. Two approaches are discussed, one with a fixed difference in the ascending nodes and one with a drifting difference. Both approaches provide a full two-dimensional pattern measurement in azimuthal and polar angle. The fixed approach is faster but requires a few more active orbit maneuvers of the measurement satellite. A third approach provides elevation angle cuts at different azimuth angles. It is particularly advantageous for feed-array-reflector based digital beamforming systems, but is also of interest for classical SAR systems. A quantitative example is provided for an L-band SAR system with digital beamforming, i.e., Tandem-L. Orbit simulations verify the proposed approaches.

1 Introduction

Digital beamforming will be an integral part of many future SAR missions. SCan On REceive (SCORE) is one example, e.g. [1], [2], [3]. In Tandem-L, a 2D-feed array is combined with a large 15-m-reflector [3], and a digital SCORE operation in elevation is linked with different analog fixed feed-array settings in azimuth. The system is designed for single-, dual- and quad-polarization. The feed array consists of 6 azimuth x 35 elevation elements. Each feed element illuminates via the reflector a different but adjacent area on the ground. Due to the fixed azimuth settings, 35 individual elevation channels are input to the on-board digital beamforming. For SCORE, the received signals of a varying number of adjacent feed-array elevation elements are digitally combined to form multiple beams that follow the echo on ground [3]. A sketch of a Tandem-L like antenna system with a small measurement satellite as is discussed in this paper is shown in Figure 1.

Unlike in phased-array systems, the single element secondary patterns, i.e. feed array element plus reflector, are different from each other and need individual measurements with high accuracy in amplitude and phase, also beyond the 3dB-width and into the sidelobe area. This applies even more to Tandem-L, which has been designed for multiple elevation beams and staggered SAR operation that both make the system vulnerable to range ambiguities [4].

Sufficient pattern measurement with the radar satellite in space can be achieved for phased antenna arrays with the established ground calibration approach based on ground targets and elaborated antenna models [5],[6],[7]. For the antenna models, element pattern measurements can be obtained on-ground before launch. However, a measurement of the secondary element beams in case of large reflectors can hardly be realized before launch, simply due to the large dimensions. On top of this, the secondary element patterns are not separable into azimuth and elevation beams [4]. Further, the feed-array-reflector geometry in space and after a potential reflector unfolding will deviate from that before launch on ground. The measurement of the secondary far field pattern of individual feed-elements by using ground targets is further limited by the acquisition geometry.

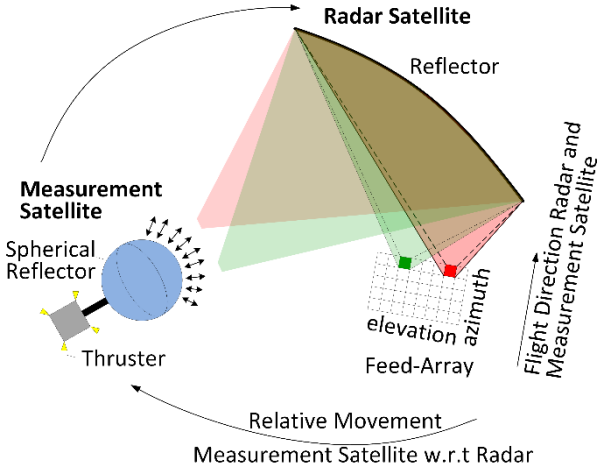

Figure 1 Two-way pattern measurement for a radar SAR satellite (RSS) with two-dimensional feed-array and large parabolic reflector by means of a small measurement satellite (MES). Feed-array depiction adapted from [3].

With ground targets, it is also not possible to measure angles beyond the main-lobe in azimuth as well as in elevation. A 2D measurement of the patterns is not possible, only the azimuth pattern in receive can be measured in high angular sampling by a ground receiver, and only the two-way pattern in elevation can be measured, whereby for each elevation sample a dedicated ground target is required. Rain forest measurements allow for highly sampled elevation patterns, but suffer, e.g., from ambiguities.

In [4], a technique for the estimation of the individual feed-array element's relative secondary far field patterns is proposed with the radar satellite in-orbit. It is based on calibration flights over natural acquisition areas with known topography in a transparency mode where the signals of one or more individual feed-array elements are recorded and downlinked without any on-board digital beamforming, i.e., each channel is downlinked separately. From a series of those calibration flights the relative secondary far field patterns are estimated. The challenges of this technique are the high downlink volume and/or reduction of the signal (chirp) bandwidth to reduce the data rate [4]. The major disadvantage is that only one of the many patterns can be measured during one overflight. A pulse-wise electronic switching of many patterns would reduce the PRF

Proceedings EUSAR 2024, pp1232-1237, ISBN 978-3-8007-6286-6, ISSN 2197-4403.

and thus extremely increase the azimuth ambiguities. Further, all the distortions known from SAR data acquisition apply, which include atmospheric and ground distortions. Due to ambiguities and SNR limitations, meaningful far field element pattern measurements can only be obtained in the high gain areas of the main peak.

Recently, a novel approach for the 2-D in-orbit antenna pattern measurement by means of a dedicated small measurement satellite that flies in close formation with the SAR satellite has been proposed [8]. It allows for a full two-dimensional (2D) antenna pattern measurement up to ±90° angular range. The Double-Cross-Helix formation [8] shapes the geometry between radar and measurement satellite in such a way that during one orbit period one central cut of the two-dimensional antenna pattern is obtained. Since this means a slow scan along the central cut, many antenna patterns can be measured interleaved by switching them electronically in the course of the orbit.

In this paper, the radar SAR satellite (RSS) parameters of Table 1 are used. They are based on the Tandem-L mission proposal of DLR [3]. The parameters of the measurement satellite (MES) are with respect to the RSS ones.

Table 1 Parameters for the RSS and MES satellites.

	RSS		MES	
semi-major axis	a_{RSS}	7123 km	a_{MES}	$= a_{RSS}$
argument of perigee	ω_{RSS}	90°	ω_{MES}	$= \omega_{RSS}$
eccentricity	e_{RSS}	0.001036	e_{MES}	$= e_{RSS} + \Delta e$
inclination	i_{RSS}	98.373°	i_{MES}	$= i_{RSS} + \Delta i$
ascending node	Ω_{RSS}	90°	Ω_{MES}	$= \Omega_{RSS} + \Delta\Omega$
time at central orbit position (COP)	τ_{RSS}	0 s	τ_{MES}	$= \tau_{RSS} + \Delta\tau$
side-looking offset (right)	θ_{off}	33.5°		
radar center frequency	f_0	1.258 GHz		
diameter radar reflector		15 m		

2 Double-Cross-Helix Measurement

As shown in Figure 1, the measurement satellite MES is equipped with a spherical reflector that permanently faces the parabolic reflector of the radar SAR satellite RSS. The spherical reflector provides several benefits. Its small radar cross section supports short distance measurements in regard of high radar power. Its reflection is direction-independent, and it shields the MES's bus from radar illumination. Both satellites fly approximately the same orbit, but small differences in the MES's orbit parameters adjust a Double-Cross-Helix formation. In this formation, MES fully revolves RSS during one orbit in all the three dimensions along-track, cross-track, and radial of the RSS local coordinate system.

The well-known helix-orbit of the Tandem-X mission [9],[10] that is generated by differences in the eccentricities Δe (along-track and radial baseline components [12]), and the ascending nodes $\Delta\Omega$ (cross-track component) also results in a full revolution. However, as is derived in [8], a second cross-track baseline component generated by a difference in the inclinations Δi is required to consider the side-looking SAR geometry. Figure 2 illustrates the two cross-track baseline components and its generating orbit parameter differences.

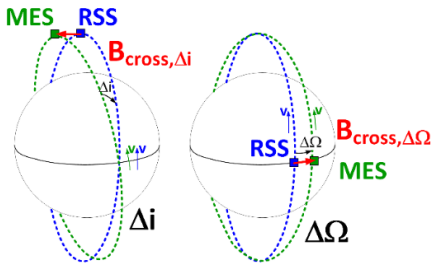

Figure 2 Illustration of the two across-track baseline components in the RSS *local system* that are generated by an inclination difference (left) and a difference in the ascending nodes (right). The argument of perigee ω is 90°.

In Figure 1 and the paper, a two-way measurement is discussed. Of course, one-way measurements of individual transmit and receive patterns can be achieved with the same orbit geometry. For this, the MES in Figure 1 could, e.g., be turned by 180° and a transmitting/receiving antenna could be attached to the side then facing the RSS.

2.1 Antenna Pattern Central Cut Geometry

Figure 3 shows the Cartesian and spherical radar antenna pattern coordinate systems. The superscripts in the axes x^A, y^A, and z^A designate the *Antenna system*.

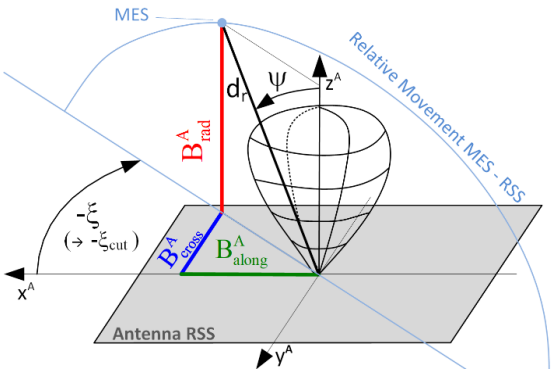

Figure 3 RSS Cartesian Antenna coordinate system A and related spherical system. Relative position of MES to antenna center in the baseline components B^A_{along}, B^A_{cross}, and B^A_{rad}. The relative movement in one orbit supplies a pass of polar angles ψ at a fixed azimuthal angle ξ.

With (1), the spherical coordinates radial distance d, polar angle ψ and azimuthal angle ξ can be calculated from the baseline components. The measurement considers the antenna pattern to be two-dimensional in ψ and ξ. At each measurement position, the distance d is available from the orbit geometry and thus known with high accuracy.

$$\sin\xi = \frac{B^A_{cross}}{\sqrt{\left(B^A_{along}\right)^2 + \left(B^A_{cross}\right)^2}} \quad ; \xi \in [-90°, 90°[$$

$$\tan\psi = \frac{\sqrt{\left(B^A_{along}\right)^2 + \left(B^A_{cross}\right)^2}}{B^A_{rad}} ; \psi \in [-90°, 90°] \qquad (1)$$

$$d = \sqrt{\left(B^A_{along}\right)^2 + \left(B^A_{cross}\right)^2 + \left(B^A_{rad}\right)^2}$$

The MES orbit parameters are derived for a relative movement w.r.t. RSS that transits all polar angles ψ at a constant azimuthal angle ξ. Figure 3 illustrates this movement by the blue bow. Setting different measurement satellite's orbit parameters results in different central cuts, i.e., different azimuthal angles ξ.

2.2 Central Cut Approaches

There are two approaches to calculate the required orbit parameters that adjust central cuts [8]. The *fixed-$\Delta\Omega$* approach sets first a fixed value for the ascending nodes difference $\Delta\Omega$ based on a required minimum distance between the satellites. In this paper, a 2 km minimum distance is desired, which corresponds to a fixed $\Delta\Omega$ of 73.2 mdeg for the parameters of Table 1. For more details please refer to [8]. The *drifted-$\Delta\Omega$* approach exploits the difference in the ascending node drift rates that is due to a difference in the radar and measurement satellite's inclinations Δi.

2.2.1 Fixed-$\Delta\Omega$ Calculation Approach

The required differences in the orbit parameters eccentricity Δe, inclination Δi, ascending node $\Delta\Omega$, and also a fourth required orbit parameter, the orbit time difference at the RSS Central Orbit Position (COP) $\Delta\tau$ are derived in [8]. The COP is either the perigee or the apogee of the radar satellite's orbit. At this position, the along-track and the cross-track components of the baseline in the *Antenna system* become zero, while the radial component is positive. The desired orientation of the MES spherical reflector towards the radar reflector goes along with a positive radial baseline component. For this reason, the measurement of a central cut at negative azimuthal angles ξ needs to be around perigee, and at positive ones, the measurement needs to be around apogee. For a desired azimuthal angle ξ, the required eccentricity and inclination differences can be calculated with (2) and then with (3).

$$\Delta e \approx -\frac{\sin i_{RSS}\cdot\left(1-e_{RSS}^2\right)\cdot\sin\Delta\Omega\cdot\cos\theta_{off}}{2\cdot\tan\xi} \tag{2}$$

$$\Delta i \approx (-1)\cdot\operatorname{asin}\left(\frac{\tan\theta_{off}\cdot\Delta e}{1\mp\left(e_{RSS}+\Delta e\right)}\right) \tag{3}$$

In (3), the upper and lower signs are for $\xi < 0$ and $\xi > 0$. The subscript RSS indicates parameters of the radar satellite RSS. The small orbit time shift $\Delta\tau$ adjusts the *Antenna system's* along-track baseline at perigee/apogee to zero.

$$\begin{aligned}\Delta B_{along}^{L} &\approx -a\cdot\left(1\mp\left(e_{RSS}+\Delta e\right)\right)\cdot\sin\left(i_{MES}-90°\right)\cdot\sin\Delta\Omega\\ \Delta\tau &= -\Delta B_{along}^{L}\cdot v_s\end{aligned} \tag{4}$$

In (4), a is the semi-major axis that is identical for RSS and MES, and v_s is the satellite velocity at COP.

Due to the $\tan\xi$-term in the denominator of (2), an azimuthal angle ξ close to 0° is not allowed to prevent from a too large eccentricity difference Δe that would cause too large baselines. Likewise, ξ-values too close to ±90° cause Δe to vanish, which means too similar and thus insecure RSS and MES orbits in terms of *local systems* radial and along-track baselines. In order to keep ξ away from these extreme values, an azimuthal offset angle ξ_{off} is introduced, which rotates the radar satellite around its antenna z-axis. This splits the azimuthal angle ξ in (5) into two parts, i.e., an azimuthal cut angle ξ_{cut} and an azimuthal offset angle ξ_{off}. By doing so, the azimuthal angle of the central cut in Figure 3 becomes ξ_{cut}, and the azimuthal angle ξ in the equations above is within save limits. Figure 4 (a) provides the ξ_{off} angles as applied in the paper's example.

$$\xi = \xi_{cut} + \xi_{off} \Leftrightarrow \xi_{cut} = \xi - \xi_{off} \tag{5}$$

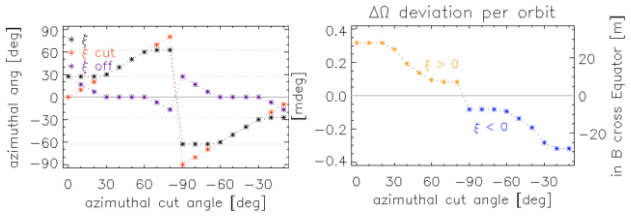

(a) (b)

Figure 4 (a) Azimuthal offset angles ξ_{off} for cut angles ξ_{cut} in 10°-steps and resulting ξ as input to the equations. (b) Deviation from the fixed $\Delta\Omega$ –value per orbit due to the difference in Δi. The right vertical axis provides the deviation converted into cross-track baseline at the equator.

In the end, a small numerical correction of Δi and $\Delta\tau$ is added that is due to the approximations required in the derivations [8], which are in the order of 0.03 mdeg and 1 ms, respectively.

The inclination difference Δi causes a small drift in the difference of the ascending nodes $\Delta\Omega$ [8] that is in the order of 0.2 mdeg per orbit as shown in Figure 4 (b). This can be considered by small $\Delta\Omega$ updates in (2) and (4). A 2D measurement lasts a few days.

2.2.2 Drifted-$\Delta\Omega$ Calculation Approach

The drift effect is exploited, which increases the measurement time for a two-dimensional measurement to a few months, but decreases the required ΔV. The differences in Δe and Δi are kept fixed. Due to the drift in $\Delta\Omega$, the desired azimuthal angles ξ adjust after particular times. The detailed derivation can be found in [8]. Here, a brief summary is provided. The measured azimuthal angle ξ can be expressed as a function of the number of drifted orbits $n_{drifted}$ counted from the measurement start with a $\Delta\Omega_{\text{start}}$.

$$\begin{aligned}\tan\xi\left(n_{drifted}\right) &\approx \frac{\sin i_{RSS}\cdot\left(1-e_{RSS}^2\right)\cdot\sin\theta_{off}}{2}\cdot\frac{\Delta\Omega_{start}+\Delta\dot{\Omega}\cdot T_{orbit}\cdot n_{drifted}}{\Delta i}\\ \Delta\dot{\Omega} &\approx k_{\Omega}\cdot\Delta i\\ k_{\Omega} &= +\frac{3}{4}\cdot J_2\cdot\sqrt{\frac{\mu}{a^3}}\cdot\left(\frac{r_{E,equator}}{a\cdot\left(1-e_{RSS}^2\right)}\right)^2\cdot\left(2-\left(i_{RSS}-\frac{\pi}{2}\right)^2\right)\end{aligned} \tag{6}$$

T_{orbit} is the orbit period, $r_{E,equator}$ the Earth radius at equator, and J_2 is the J_2-term of the geopotential. $\Delta\Omega_{start}$ can be calculated from the minimum required distance between the satellites, i.e. 2 km for the example, and the offset ξ_{off} at ±90° azimuthal angle (c.f. Figure 4). The inclination difference Δi results from setting $n_{drifted}$ to zero

$$\Delta i \approx \frac{\Delta\Omega_{start}\cdot\sin\left(i_{RSS}\right)\cdot\left(1-e_{RSS}^2\right)\cdot\sin\theta_{off}}{2\cdot\tan\xi_{start}}, \tag{7}$$

and the eccentricity difference Δe is then

$$\Delta e \approx \frac{-\sin\Delta i\cdot\left(1\mp e_{RSS}\right)}{\tan\theta_{off}\mp\sin\Delta i} \tag{8}$$

with the upper signs for $\xi \le 0$ and the lower ones for $\xi > 0$. The drifted orbits number as a function of the desired ξ is

$$n_{drifted}\left(\xi\right) = \frac{2\cdot\left(\tan\xi-\tan\xi_{start}\right)}{\sin\left(i_{RSS}\right)\cdot\left(1-e_{RSS}^2\right)\cdot\sin\theta_{off}\cdot k_{\Omega}\cdot T_{Orbit}} \tag{9}$$

2.2.3 Results for Fixed- and Drifted-$\Delta\Omega$ Approaches

The Double-Cross-Helix parameters were calculated for the L-band system parameters of Table 1 in steps of 10° of azimuthal cut angle ξ_{cut}. Then the orbits were simulated,

the *local* and *antenna system* baselines were computed, and finally the azimuthal cut angle ξ_{cut}, the polar angle ψ, and the antenna pattern azimuth θ_{az} and elevation θ_{el} angles were calculated. The latter two can also be estimated from the baseline components in the *antenna system* [8].

$$\sin\theta_{el} = \frac{-B^A_{cross}}{\sqrt{\left(B^A_{cross}\right)^2 + \left(B^A_{rad}\right)^2}} \quad ; \sin\theta_{az} = \frac{B^A_{along}}{d \cdot \cos\theta_{el}} \tag{10}$$

Figure 5 provides the differential orbit parameters for the fixed $\Delta\Omega$–approach that adjust the azimuthal cut angles ξ_{cut}. The x-axes are organized in the sequence of ξ_{cut} measurements; first from 0° to the largest positive $\xi_{cut} > 90°$, and then from -90° to the largest negative $\xi_{cut} < 0°$.

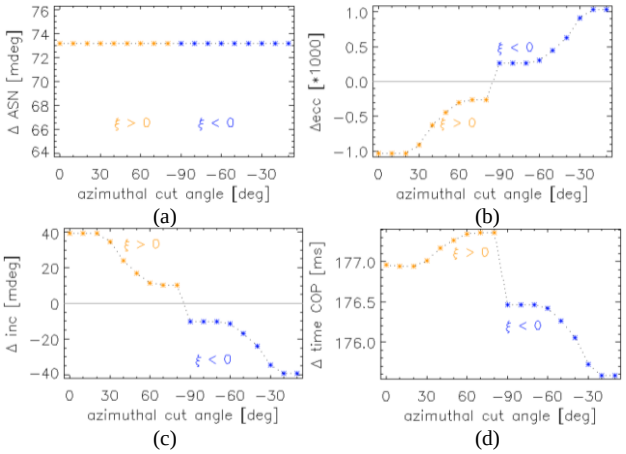

Figure 5 Differential parameters for fixed $\Delta\Omega$ approach. (a) Ascending nodes $\Delta\Omega$, (b) eccentricity Δe, (c) inclination Δi, and (d) time at central orbit position $\Delta\tau$ at COP.

The baseline components in the local and antenna systems that result from the differential orbit parameters provide a deeper insight into the Double-Cross-Helix concept, but for a more in-depth discussion, please refer to [8].

For the drifted $\Delta\Omega$ approach, the first important result is the number of drifted orbits $n_{drifted}$ until a desired ξ_{cut} can be measured, i.e., until the proper ascending node difference $\Delta\Omega$ adjusts. Due to the identical azimuthal angles ξ (cf. Figure 4), the first azimuthal cut angles -90°, -80° and -70° in Figure 6 are measured in consecutive orbits with identical orbit parameters. After about 100 orbits, ξ_{cut} = 60° is measured. Before measuring ξ_{cut} = 0°, Δi, and Δe are switched in sign for positive ξ-values (cf. Figure 7). This means a reversal of the $\Delta\Omega$ drift direction.

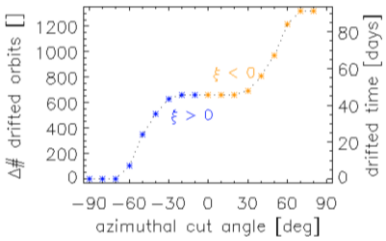

Figure 6 Number of drifted orbits until $\Delta\Omega$ adjusts for a next ξ_{cut}. Right vertical axis provides the duration in days.

Figure 7 provides the parameters for the drifted $\Delta\Omega$-approach. Due to the sign-change of Δi, the decrease in $\Delta\Omega$ changes to an increase for positive ξ_{cut}. A full 2D-measurement lasts 93 days, also in case of a denser ξ_{cut} -sampling.

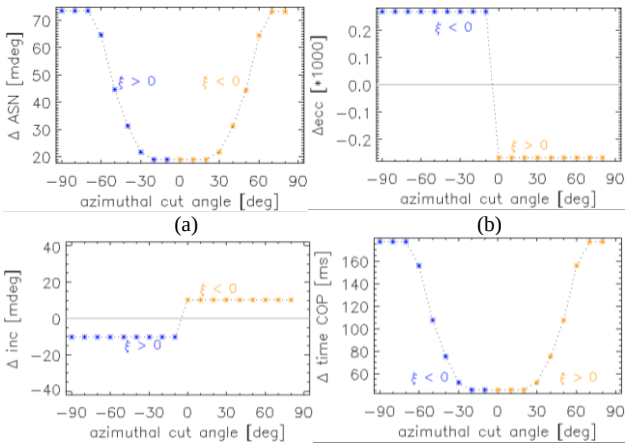

Figure 7 Differential parameters for drifted $\Delta\Omega$-approach. Note the different sequence on the ξ_{cut}-axes w.r.t. Figure 5.

Figure 8 provides the measurement angles from the fixed $\Delta\Omega$ approach. The results for the drifted approach are identical. Plot (c) provides additional 1°-steps in a ±5° range around ξ_{cut}=0°, and a ±10° range around ξ_{cut}=90° (dotted).

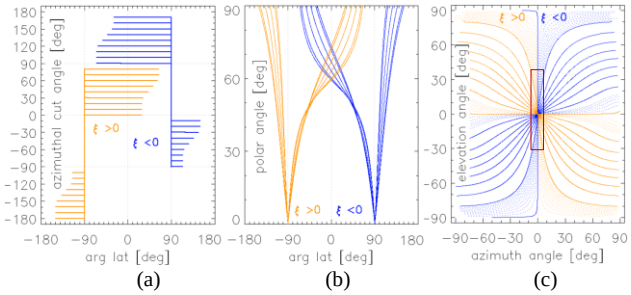

Figure 8 Fixed $\Delta\Omega$ approach measurement angles. (a) azimuthal cut, (b) polar, (c) azimuth and elevation angles.

Figure 9 provides for the fixed and drifted approaches a first estimation of the ΔV required to change the MES orbits with non-combined maneuvers. A fixed approach 2D measurement is faster. In case of 10° steps and updating the MES parameters each orbit it lasts 29 hours. The drifting approach lasts 91 days. A higher ξ_{cut} sampling increases the duration of the fixed approach but not of the drifted one. The required ΔV does not increase for both.

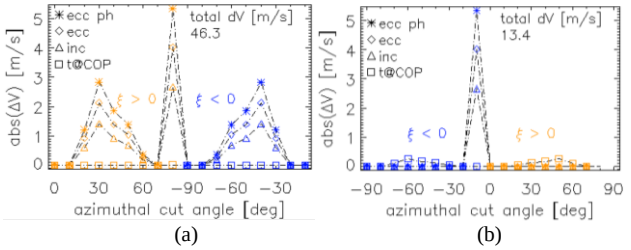

Figure 9 ΔV for 2-D measurement in 10°-steps, e.g., ΔV at 30° is for change to 40°. Eccentricity (ecc), phasing after ecc. (ecc ph), inclination (inc), and Δt. Fixed (a) and Drifted (b) $\Delta\Omega$ approach.

3 Two-Dimensional Feed-Array

The third approach calculates MES orbits in such a way that the cuts are very close to elevation patterns, i.e., traversing elevation angles at almost constant azimuth angles. It is advantageous if an accurate 2-D pattern is required in a central region of the pattern, e.g., for the derivation of

optimum beamforming coefficients, which then allow for a smaller reflector size. In the Tandem-L example of Figure 8 (c), the red central high accuracy measurement region extends ±35° in elevation angle and ±3° in azimuth, i.e., beyond the nadir-direction at 33° elevation angle, and beyond the second azimuth pattern side lobes, respectively.

3.1 Elevation Patterns Measurement

The Double-Cross-Helix fixed approach is modified. The measurement orbit for ξ_{cut} = -90° is used repeatedly. It provides the central cut elevation pattern. An additional rotation of the RSS satellite by a delta azimuth angle $\Delta\theta_{az}$ around the antenna system y^A-axis is introduced before the final RSS rotation by ξ_{cut} around the z^A-axis (cf. [8]). Figure 10 illustrates the $\Delta\theta_{az}$-rotation. The violet curve shows the relative MES movement without $\Delta\theta_{az}$, and the brown curve with additional $\Delta\theta_{az}$. As well as the ξ_{cut}-rotation, the $\Delta\theta_{az}$-rotation is realized by updating the RSS attitude steering angles. Figure 11 shows for initial RSS attitude angles of zero the resulting yaw (b), pitch (c), and roll angles (d) for a constant ξ_{off} of 27° and $\Delta\theta_{az}$ values that increase from -3° in steps of 0.1° to +3°. With regard to the large reflector structure, the change in the attitude angles from orbit to orbit is very small and steady.

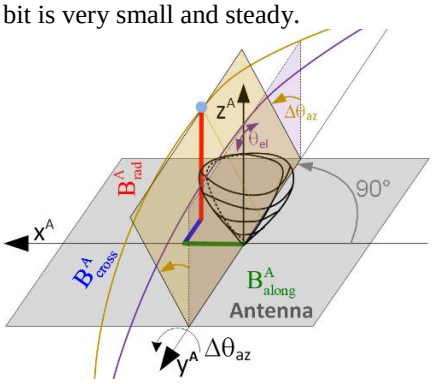

Figure 10 Elevation patterns measurement by additional rotation around antenna system y^A-axis. Relative movement of the MES satellite in violet color for zero $\Delta\theta_{az}$, and in brown color for a non-zero $\Delta\theta_{az}$.

For the elevation pattern approach, the numerical update (cf. [8]) is adapted by substituting the updates in orbit time $\Delta\tau$ and inclination Δi differences by a numerical update of $\Delta\theta_{az}$. The RSS and MES orbits are simulated, the baseline components at COP are measured, and the residual delta azimuth angle $\Delta\theta_{az,res}$ is estimated from the residual along-track baseline $B^A_{COP,along,res}$, i.e. the difference between the $B^A_{COP,along}$ expected for $\Delta\theta_{az}$ and the measured one. Then, $\Delta\theta_{az,res}$ is subtracted from $\Delta\theta_{az}$ in the next iteration.

$$\Delta\theta_{az,res} = \arcsin\left(\frac{-B^A_{COP,along,res}}{\cos\theta_{el,res}\cdot\sqrt{\left(B^A_{COP,along}\right)^2+\left(B^A_{COP,cross}\right)^2+\left(B^A_{COP,rad}\right)^2}}\right)$$
$$\text{with } \theta_{el,res} = \operatorname{asin}\left(\frac{-B^A_{COP,cross}}{\sqrt{\left(B^A_{COP,cross}\right)^2+\left(B^A_{COP,rad}\right)^2}}\right) \quad (11)$$

Figure 11 (d) provides the resulting updated $\Delta\theta_{az}$ together with the desired value. The simulations were performed with the parameters of the fixed approach, and the resulting orbit parameters can be found in Figure 5 at ξ_{cut} = -90° on the abscissa.

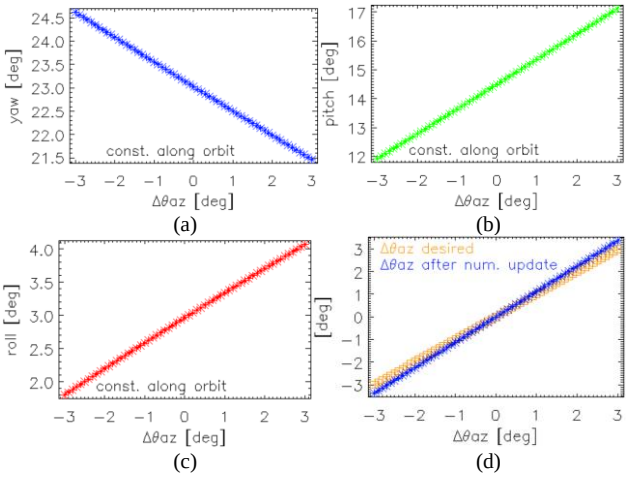

Figure 11 Yaw (a), pitch (b), and roll angles (c) to rotate the RSS satellite by ξ_{cut} = 27° around the antenna z-axis and by a $\Delta\theta_{az}$ ranging from -3° to +3° in steps of 0.1°. (d) Desired and final $\Delta\theta_{az}$ values after the numeric iteration.

Since all the MES orbit parameters are kept constant there is no ΔV required. Nevertheless, a small ΔV must be spent to keep the difference in the ascending nodes $\Delta\Omega$ constant. The Δi of 10.2 mdeg results in a difference in the RSS and MES drifts of 0.0825 mdeg/orbit. The accumulation for 61 measurement orbits results to 5 mdeg. Since $\Delta\Omega_{Drift}$ is small, both values can be converted [13] into the required $\Delta V_{\Delta\Omega,Drift,correction}$ to compensate the drift difference. It results to 10.68 mm/s in one orbit and to 0.65 m/s for all 61 measurement orbits. V_s is the satellite velocity. Figure 12 provides finally the measurement angles.

$$\Delta V_{\Delta\Omega,Drift,correction} \approx V_s \cdot \sin i_{RSS} \cdot \Delta\Omega_{Drift}\,, \quad (12)$$

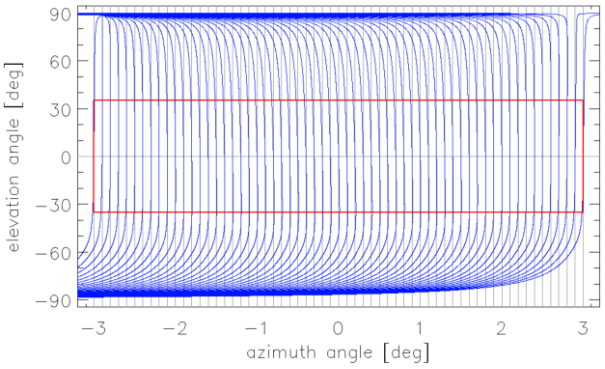

Figure 12 Measurement angles estimated from orbit simulations for desired $\Delta\theta_{az}$ from -3° to +3° in steps of 0.1°.

3.2 Concurrent Patterns Measurement

A power calculation with the Tandem-L parameters [3] showed that one measurement pulse, i.e., one azimuth pulse, is sufficient to achieve a SNR of 35 dB for a bandwidth of 85 MHz, and a partial pulse integration of 0.33 µs out of a full pulse of 9.52 µs. The partial integration moves along the full pulse length and thus keeps the inherent frequency dependency of the antenna pattern measurement by using, e.g., a chirp waveform [8]. So, the burst length required to measure at one elevation angle position equals 1/PRF, e.g., 0.24 ms for a PRF of 4200 Hz. Note, this value is not necessarily related to the Tandem-L system PRF.
As can be observed in Figure 13 (a), for constant orbit time sampling intervals, the elevation angle sampling interval

varies due to the orbit geometry. If equidistant elevation angle sampling intervals are desired, the sampling time interval varies. Figure 13 (b) shows for 0.01° elevation angle sampling at $\Delta\theta_{az}$ = 3° and ξ_{cut} = 27° the time sampling interval in red color, and in blue color the length of a measurement burst, i.e. 1/PRF. The minimum gap is 32.77 ms.

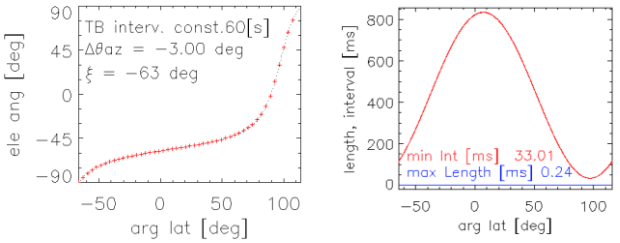

(a) (b)

Figure 13 (a) Elev. angle for $\Delta\theta_{az}$ = -3° and ξ_{cut} = 27° (ξ = 63°) for equidistant time interval of 60 s. (b) Varying time sampling for constant elevation angle sampling of 0.01°. Min. gap between burst interval and length is 32.77 ms.

In the time gap between two measurement bursts the secondary element patterns of different feed array elements can be measured. The concurrent measurement is with identical azimuth offset angle $\Delta\theta_{az}$ for all electronically switched feed elements. Dividing the minimum gap by the measurement burst length results in 137 secondary feed array element patterns that can be concurrently measured (1370 patterns for 0.1° sampling). Note that ground echoes can be avoided by appropriate timing. For the Tandem-L example, this means that the 70 secondary far field elevation element patterns (35 in H- and 35 in V-polarization) can be measured in the same orbit at the same azimuth angle. After 61 orbits covering all different $\Delta\theta_{az}$ angles in a 0.1° sampling, the 2D measurement of the central region of the antenna pattern in azimuth/elevation angle can be completed with a small required ΔV = 0.65 m/s.

4 Conclusion

Fixed and drifted approaches of the in-orbit antenna pattern measurement by using a small measurement satellite flying in Double-Cross-Helix formation were introduced. For the discussed Tandem-L example, both approaches provide a full 2-D pattern measurement in azimuthal and polar angle. A third approach was proposed that measures elevation angle cuts at different azimuth angles. The modifications of the approach w.r.t. the fixed approach were discussed. Since the same measurement orbit is constantly used, the required ΔV restricts to counterbalancing the difference in the ascending node drifts that is due to the inclination difference Δi. In the example, ΔV results to 0.65 m/s for the required 61 measurement orbits. The slow change of the elevation (or polar) measurement angle allows the concurrent measurement of many patterns at the same fixed azimuth (or azimuthal) angle. For Tandem-L, all the 70 feed-array secondary far field element patterns can be measured easily in one orbit at the same azimuth angle position with high elevation angle sampling. The in-orbit two-dimensional pattern measurement with the Double-Cross-Helix formation is a free-space measurement and thus avoids all the distortions that are involved in a measurement with ground-based equipment, e.g., atmosphere, ionosphere, ground clutter or multipath effects, ambiguities, and volume scattering. The thus highly accurate measurement allows to measure also the antenna phase pattern and exact polarimetric patterns. The phase patterns are required for the derivation of optimized beamforming coefficients.

5 Acknowledgement

The authors want to thank Sigurd Huber for helpful discussions related to Tandem-L.
Co-funded by the European Union (ERC, DRITUCS, 101076275). Views and opinions expressed are however those of the authors only and do not necessarily reflect those of the European Union or the European Research Council Executive Agency. Neither the European Union nor the granting authority can be held responsible for them.

6 Literature

[1] M. Suess, B. Grafmueller, R. Zahn, “A novel high resolution, wide swath SAR System”, Proc. IGARSS 01.
[2] Federica Bordoni, Gerhard Krieger, “Mitigation of the SAR Image Radiometric Loss Associated with the SCORE DBF in Presence of Terrain Height Variations”, Proc. of EUSAR 2022.
[3] S. Huber et al., “Tandem-L: A Technical Perspective on Future Spaceborne SAR Sensors for Earth Observation”, IEEE TGRS, Vol. 56, No. 8, Aug. 2018.
[4] G. Krieger, S. Huber, M. Younis, A. Moreira, J. Reimann, P. Klenk, M. Zink, M. Villano, F. Queiroz de Almeida, “In-Orbit Relative Amplitude and Phase Antenna Pattern Calibration for Tandem-L”, Proc. of EUSAR 2018.
[5] T. Freeman, “SAR Calibration: An Overview,” IEEE Transactions on Geoscience and Remote Sensing, Vol. 30, pp. 1107–1121, 1992.
[6] J. Reimann, M. Schwerdt, K. Schmidt, N. Tous Ramon, B. Döring, “The DLR Spaceborne SAR Calibration Center,” Frequenz, 2017.
[7] M. Bachmann, M. Schwerdt, B. Bräutigam, “TerraSAR-X Antenna Calibration and Monitoring Based on a Precise Antenna Model,” IEEE Trans. Geosci. Remote Sensing, Vol. 48, pp. 690–701, 2010.
[8] J. Mittermayer, G. Krieger, M. Villano, “A Novel Approach for In-Orbit Satellite Antenna Pattern Measurement using a Small Satellite Flying in Double-Cross-Helix Formation”, submitted for TGRS.
[9] A. Moreira, G. Krieger, and J. Mittermayer, “Satellite configuration for interferometric and/or tomographic remote sensing by means of synthetic aperture radar (SAR)”, U.S. Patent 6 677 884 Jul. 1, 2002.
[10] R. Kahle, B. Schlepp, F. Meissner, M. Kirschner, and R. Kiehling, “The TerraSAR-X /TanDEM-X formation acquisition – From planning to realization,” *J. Astronautical Sci.*, vol. 59, pp. 564–584, 2012.
[11] S. D’Amico, O. Montenbruck, C. Arbinger, and H. Fiedler, “Formation flying concept for close remote sensing satellites,” in *Proc. 15th AAS/AIAA Space Flight Mech. Conf.*, Copper Mountain, CO, 2005, pp. 831–848.
[12] D. Massonnet, J.-J. Martin, „Radar Interferometry Device”, PCT WO 99/58997, 18.11.1999.
[13] C. Klüver, “Space Flight Dynamics”, John Wiley & Sons, LCCN 2017042818, 2018, page 316.